Ramping-based Variable-Timescale Co-optimization for Distribution Planning and Operation

Luomeng Zhang, *Student Member, IEEE*, Hongxing Ye, *Senior Member, IEEE*, Yinyin Ge, Zuyi Li, *Senior Member, IEEE*

***Abstract*—The growing penetration of distributed photovoltaic (PV) poses new challenges, such as voltage security and output uncertainty, in distribution networks. The efficient and secure integration of high-level PV has recently garnered much attention. This work proposes a novel variable timescale model for the planning-operation co-optimization, aiming to unlock more flexibility for PV integration. We introduce a novel ramp event detection algorithm to adjust timescales, focusing on critical time periods. Consequently, this allows for flexibility unlocking by adjusting high-resolution time periods with binary variables while maintaining an efficient model size. To guarantee the robustness and nonanticipativity in planning, we propose a multistage optimization model with a variable uncertainty set. A hybrid solution approach is then proposed to solve the challenging model. In the meantime, the model takes into account utilization of the mobile energy storage system (MESS). To validate the approach, we perform the case study using the 13-bus system, 141-bus system, and 906-bus system. The numerical test results demonstrate the efficiency and accuracy of the proposed methodologies.**

***Index Terms*—Variable Timescale, Ramp Event, Multistage Optimization, Surrogate Affine Policy.**

NOMENCLATURE

A. Sets and Indices

$\mathcal{T}, t$	Set/Index of time periods.
$\mathcal{N}, n$	Set/Index of PVs.
$\mathcal{L}, l$	Set/Index of MESSs.
$\mathcal{I}, i$	Set/Index of buses.
$\Theta(i), i'$	Set/Index of buses directly connected to bus i.
$\mathcal{C}, c$	Set/Index of MESS candidate locations.
$\mathcal{M}, m$	Set/Index of loads.
$\mathcal{Q}, q$	Set/Index of distribution lines.

B. Variables

P_t^b, Q_t^b	Active/Reactive power from the main grid.
$P_{i,t}^{\text{inj}}, Q_{i,t}^{\text{inj}}$	Active/Reactive power injected into bus i.
$V_{i,t}$	Voltage magnitude of bus i.
$P_{ii',t}, Q_{ii',t}$	Active/Reactive power flow on line from bus i to bus i'.
$P_{q,t}, Q_{q,t}$	Active/Reactive power flow on q-th line.
$P_{n,t}^v$	Active power output of n-th PV.
$P_{c,l,t}^{s,c}, P_{c,l,t}^{s,d}$	Charging/Discharging power of l-th MESS connected with c-th candidate location.
$P_{m,t}^d, Q_{m,t}^d$	Active/Reactive power demand of m-th load.
C_n^v, C_l^s	Installation capacity of PV/MESS.
$E_{l,t}^s$	Energy level of l-th MESS.
$\lambda_{c,l,t}$	Connected indication of c-th candidate location and l-th MESS.
$\chi_{l,t}$	Transit status of l-th MESS
$u_{n,t}^{v,low}$,$u_{n,t}^{v,up}$	Lower/Upper bound of PV uncertainty set.
$u_{m,t}^{d,low}$,$u_{m,t}^{d,up}$	Lower/Upper bound of load uncertainty set.
$P_{m,t}^{d,h}, P_{n,t}^{v,h}$	Power of load shedding/PV curtailment.
$\boldsymbol{\pi}$	Non-negative multiplier.

C. Parameters

N_n, N_m	Number of PVs/loads.
$\mathcal{W}$	Tolerance band range of critical aperture.
ν	Proportion of total PV capacity to total load for ramp event detection in planning model.
r	Annual interest rate.
y^v, y^s	Lifespan of PV/MESS.
R^v, R^s	Investment cost per unit of PV/MESS.
$r_{ii'}, x_{ii'}$	Resistance/Reactance of line from bus i to bus i'.
α_l^s	Deep of discharge of l-th MESS.
η_l^c, η_l^d	Coefficient of charging/discharging power limit of l-th MESS.
μ_l^c, μ_l^d	Charging/Discharging efficiency of MESS.
$\underline{V}, \bar{V}$	Lower/Upper limit of voltage magnitude.
$\bar{S}_q$	Apparent power capacity of q-th line.
$k_{n,t}^{low}, k_{n,t}^{up}$	Lower/Upper bound coefficient for the confidence interval of n-th PV.
$k_{n,t}^f$	Forecast expectation coefficient of n-th PV.
$P_{m,t}^{d,low}$	Lower bound for the confidence interval of load.
$P_{m,t}^{d,up}$	Upper bound for the confidence interval of load.
$P_{m,t}^{d,f}$	Forecast expectation of m-th load.
ρ^{b+}	Electricity price for buying from the main grid.
ρ^{b-}	Electricity price for selling to the main grid.
ρ^o	Transportation cost of MESS.
ρ^h	Cost of PV curtailment and load shedding.
T_{c_1,c_2}^{travel}	Travel time of MESS from node c_1 to c_2.

I. INTRODUCTION

In recent years, renewable generation, such as photovoltaic (PV), has increased significantly. However, the high penetration of PV has been posing challenges to the distribution network, such as reversed power flow, overvoltage, and real-time power balance [1]. Distribution system operators (DSOs) are responsible for providing continuous power supply with acceptable voltage and frequency. Hence, various active network management techniques have been utilized to enhance PV integration, including on-load tap-changer [2], PV inverter [3], static var compensator [4], demand response [5], etc.

This work was supported by Science and Technology Program of SGCC 5108-202416045A-1-1-ZN. The corresponding author: Hongxing Ye

L. Zhang and H. Ye are with the College of Automation Science and Engineering, and Y. Ge is with the College of Cyber Science and Engineering, Xi'an Jiaotong University, Xi'an, 710049 Shannxi, China.

Z. Li is with Department of Electrical Engineering, Zhejiang University, Hangzhou, China.

With the technical development of energy storage systems (ESS), they are increasingly becoming a primary solution for facilitating PV integration. Traditional ESS is usually installed in a fixed location, but recently, mobile energy storage systems (MESSs) have become a hotspot in the power community due to their mobility. MESS is a mobile ESS that can be transported by truck and connected to the system at different locations. There is abundant literature related to MESS planning [6]–[8] and scheduling [9]–[13]. Previous studies have demonstrated its effectiveness in improving renewable energy integration, economic operations and grid resilience [6]–[13]. Currently, MESS has a relatively high investment cost and short lifespan. However, with technological advancements, MESS is promising as an alternative to conventional ESS in distribution systems [9]. From a pragmatic perspective, the commercial applications of MESS are becoming increasingly diverse. For example, a MESS project led by Shanghai Electric Gotion New Energy Technology Co., Ltd. has been implemented to improve renewable integration and grid resilience in a distribution system in China. Toshiba Corporation has also conducted a 776 kWh MESS for peak shaving and voltage regulation in a distribution system in Spain.

However, most existing studies consider a fixed timescale over the entire time horizon, such as one hour [6], [7], [10], [11], 30 minutes [13] or 15 minutes [12]. It has been pointed out that higher time resolutions offer advantages over traditional hourly simulations in power systems [14]. However, these advantages come at the cost of a significant increase in computational burden. Determining how to select an appropriate timescale to balance the solution quality and model complexity is a significant challenge. Ref. [15] proposes an hourly unit commitment (UC) model considering intra-hour variability of renewable power and intra-hour reserves. This model can capture intra-hour renewable variability without increasing time resolution, but the flexibility is somewhat limited due to the hourly commitment schedule. Ref. [16] presents a time-adaptive UC model that considers a time horizon consisting of 24 periods with different duration. They introduce a hierarchical clustering algorithm to determine the 24 periods that capture net-demand variability. This innovative model performs better than the hourly UC model without increasing the computational burden. On this basis, Ref. [17] employs the hierarchical clustering algorithm into the intra-day UC problem to adjust the timescale. A strategy for selecting representative scheduling points is also proposed in [18] to adjust the timescale of day-ahead UC. However, uncertainty, which is a major concern in renewable integration, is not fully considered in the most variable timescale models. Additionally, these timescale adjustment methods are not appropriate for energy storage, as they ignore the net load's duration time, which is critical for storage operation. Due to State of Charge (SOC) limitations and grid security constraints, *frequent movement of MESS may needed even when the net load curve is smooth*, as will be demonstrated in the case study. Inappropriately aggregating some smooth periods may result in the underutilization of capacity. Therefore, there exists a research gap in formulating a proper variable timescale model for the energy storage system considering uncertainty.

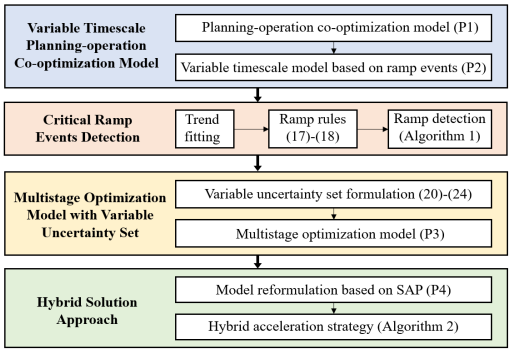

Fig. 1. Sketch of our proposed formulation.

Some studies have focused on the detection of ramp events [19]–[21] recently. Ramp event is traditionally defined as sudden and significant fluctuations of renewable resources over a short period [22]. It plays a critical role in the management and dispatch of renewable energy in the power industry [20]. When a ramp event occurs, flexible resources are employed to accommodate the fluctuation. In contrast, during non-ramp periods, the system consistently operates with relative stability, rendering these time intervals somewhat redundant. This provides a new perspective for formulating a variable timescale model. The scheduling can be tailored to prioritize ramp events, thereby preventing the need for an excessively intricate model with an excessively fine timescale. Additionally, the rules governing ramp events can be customized to align with the unique characteristics of energy storage system. This capability of detecting ramp events to contribute to the development of a variable timescale model remains unexplored in current literature.

Uncertainty has been taken into consideration recently. However, when ESS integrates into the power systems, it is challenging to find an optimal and robust scheduling and recourse action for ESS considering nonanticipativity constraints. This is mainly because of its time-coupling SOC of ESS. It has been pointed out in [23]–[26] that the existing two-stage robust method, scenario-based method, scenario-tree method, and chance-constrained model cannot guarantee the robustness and nonanticipativity of solution simultaneously. To this end, multistage optimization method proposed recently in [23]–[25] provides an effective approach for ESS to mitigate uncertainty while ensuring nonanticipativity and robustness. There are two mainstream methods to derive such decisions: explicit decision rules [24], [25] and implicit decision rules [23], [26]. Faced with realistic distribution systems with massive loads, implicit decision method could be computationally very challenging, as its scenario number will grow exponentially with uncertainty number. In the latest research, the multistage model with explicit decision rule has been applied in the MESS scheduling with renewable penetration [9]. However, in the planning model, the uncertainty set of renewable generation varies with the installation capacity of PV. It makes the multistage explicit decision methods computationally intractable [9], [24], [25]. In [27], surrogate affine policy (SAP) is proposed to address the computational challenges caused by variable uncertainty set in a two-stage model.

Ref. [28] employs SAP to increase the uncertainty-proof PV hosting capacity with a two-stage model. Nevertheless, its application to the multistage model has not been investigated. In addition, the SAP-based model is traditionally solved by the duality-based approach [27], [28], which may face scalability issues when applied to large-scale power systems. The existing literature has not resolved the scalability challenge of the SAP-based model.

The motivation of this paper is to promote renewable integration with energy storage system, considering solution robustness, nonanticipativity and computational tractability. Fig. 1 shows the sketch of this work. The contributions of this paper are threefold.

- A novel ramping-based variable-timescale model is proposed for the co-optimization of distribution planning and operation. The time resolution of the operation stage varies based on ramp events. The timescale variability provides a good balance of model accuracy and size, especially for the system with ramping events. The integer variable, i.e. MESS connecting action, can unlock flexibility by leveraging high-resolution timescale while maintaining an efficient model size.
- A general efficient approach is proposed to detect critical ramp events, enabling high-resolution timescale for the pivotal time periods. In order to capture MESS's transit periods, we also present a group of ramp rules by exploiting the characteristics of MESS. The ramping detection approach can also contribute to the compression of the high-volume power data.
- This paper introduces a novel multistage optimization model with a variable uncertainty set, and an accelerated solution approach. The uncertainty set becomes variable when the model considers the optimal PV installation capacity, PV curtailment and load shedding. To address the computational challenges, we develop a hybrid solution approach to solve the model efficiently. It provides better computational performance by integrating SAP, scenario generation and duality-based approach with various algorithmic enhancements.

The rest of this paper is organized as follows. In Section II, the variable timescale planning-operation co-optimization model is proposed. In Section III, the ramp events detection approach is presented. In Section IV, we present the multistage optimization model with a variable uncertainty set. In Section V, the hybrid solution approach is proposed. Case studies are given in Section VI. Section VII concludes this paper.

II. Variable Timescale Planning-Operation Co-Optimization Model

In this section, we first present the deterministic planning-operation co-optimization model. The model diagram is shown in Fig.2. The objective is to minimize planning and operation costs. Installation capacities of MESS and PV are decision variables at the planning level. MESS mobility, MESS charging/discharging power, PV output, power flow, node voltage, PV curtailment, load shedding, energy transactions with main grid are decision variables at the operation level. Then, a variable timescale model is formulated.

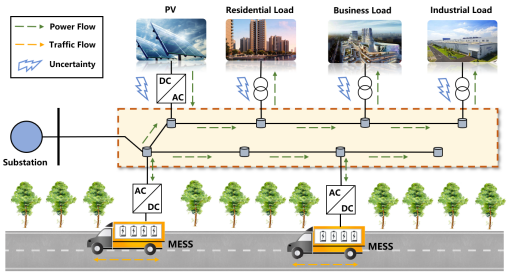

Fig. 2. Diagram of distribution system with PV and MESS.

A. Deterministic Planning-Operation Co-Optimization Model

1) MESS Constraints: MESS travels and delivers power among different nodes. MESS's temporal-spatial behavior contains transit state and parking state. The transit state represents that MESS travels from one node to the other one in a time slot. While the parking state indicates that the MESS stays at the same node in a time slot. Following [29], we present the mobility constraints for MESS as follows

$$\sum_{c\in\mathcal{C}} \lambda_{c,l,t} \le 1, \forall t \in \mathcal{T}, \forall l \in \mathcal{L}, \tag{1}$$

$$\lambda_{c_1,l,t+\tau} + \lambda_{c_2,l,t} \le 1, \forall t, t+\tau \in \mathcal{T}, \forall c_1, c_2 \in \mathcal{C}, \quad \forall l \in \mathcal{L}, \forall \tau \le T^{travel}_{c_1,c_2}, \tag{2}$$

$$\chi_{l,t} = 1 - \sum_{c\in\mathcal{C}} \lambda_{c,l,t}, \forall t \in \mathcal{T}, \forall l \in \mathcal{L}. \tag{3}$$

Constraint (1) indicates that each MESS can be connected to at most one node at each period. Constraint (2) guarantees that MESS satisfies the prescribed travel time among various nodes. Constraint (3) represents the transit status of MESS. Power and energy constraints for MESS are formulated as

$$E^s_{l,t+1} = E^s_{l,t} + \sum_{c\in\mathcal{C}} (\mu^c_l P^{s,c}_{c,l,t} - \frac{P^{s,d}_{c,l,t}}{\mu^d_l})\Delta t, \forall t \in \mathcal{T}, \forall l \in \mathcal{L}, \tag{4}$$

$$(1-\alpha^s_l)C^s_l \le E^s_{l,t} \le C^s_l, \forall t \in \mathcal{T}, \forall l \in \mathcal{L}, \tag{5}$$

$$0 \le P^{s,d}_{c,l,t} \le \eta^d_l \lambda_{c,l,t} C^s_l, \forall t \in \mathcal{T}, \forall l \in \mathcal{L}, \forall c \in \mathcal{C}, \tag{6}$$

$$0 \le P^{s,c}_{c,l,t} \le \eta^c_l \lambda_{c,l,t} C^s_l, \forall t \in \mathcal{T}, \forall l \in \mathcal{L}, \forall c \in \mathcal{C}. \tag{7}$$

Constraints (4) and (5) denote the evolution and limit of MESS energy level, respectively. Constraints (6) and (7) describe the discharging and charging power limit, respectively. Big-M method could be used to linearize constraints (6)-(7).

2) Power Flow Constraints: Linear DistFlow model has been applied to various optimization models of distribution system [9], [30], [31]. Hence, this paper uses the linear DistFlow model to convexify AC power flow equations.

$$P^{\text{inj}}_{i,t} = \sum_{i'\in\Theta(i)} P_{ii',t}, \forall i \in \mathcal{I}, \forall t \in \mathcal{T}, \tag{8}$$

$$Q^{\text{inj}}_{i,t} = \sum_{i'\in\Theta(i)} Q_{ii',t}, \forall i \in \mathcal{I}, \forall t \in \mathcal{T}, \tag{9}$$

$$V_{i,t} = V_{i',t} + (r_{ii'}P_{ii',t} + x_{ii'}Q_{ii',t})/V_1, \forall i \in \mathcal{I}, \forall t \in \mathcal{T}. \tag{10}$$

Constraints (8)-(9) build a connection between the nodal power injections and the power flows. Constraint (10) denotes the voltage drop in lines. As a side note, power flows and voltage magnitudes can be described as images of nodal power injections since the distribution system is radial.

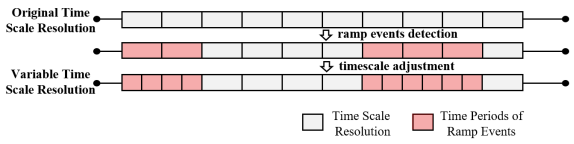

Fig. 3. Diagram of adjusting timescale based on ramp event. Timescale is refined selectively during ramp events occurring.

3) Security Constraints: This paper considers voltage limit (11) and line thermal capacity as security constraints (12). Linear box constraints [9] could be used to approximate the quadratic constraints (12).

$$\underline{V} \leq V_{i,t} \leq \bar{V}, \forall i \in \mathcal{I}, \forall t \in \mathcal{T}, \tag{11}$$

$$P_{q,t}^2 + Q_{q,t}^2 \leq \bar{S}_q^2, \forall q \in \mathcal{Q}, \forall t \in \mathcal{T}. \tag{12}$$

In the proposed co-optimization model, the objective is to minimize the total cost, which includes the investment cost, MESS transportation cost, PV curtailment cost, load shedding cost, the cost of buying electricity from main grid, and the income of selling electricity to main grid. Then, the objective function with one representative day is formulated as

$$\min \left\{ \begin{array}{l} \sum_{n\in\mathcal{N}} \rho^v C_n^v + \sum_{l\in\mathcal{L}} \rho^s C_l^s + \sum_{t\in\mathcal{T}} \sum_{l\in\mathcal{L}} \rho^o \chi_{l,t} \Delta t + \\ \sum_{t\in\mathcal{T}} \rho^h \left(\sum_{n\in\mathcal{N}} P_{n,t}^{v,h} + \sum_{m\in\mathcal{M}} P_{m,t}^{d,h} \right) \Delta t + \\ \sum_{t\in\mathcal{T}} \rho^{b+} \max\{P_t^b, 0\} \Delta t - \sum_{t\in\mathcal{T}} \rho^{b-} \min\{P_t^b, 0\} \Delta t \end{array} \right\}$$

where $\rho^v = \frac{r(1+r)^{y^v} R^v}{365[(1+r)^{y^v}-1]}$ and $\rho^s = \frac{r(1+r)^{y^s} R^s}{365[(1+r)^{y^s}-1]}$. Note that the proposed model could be generalized to consider multiple representative days per year. Then, the deterministic planning-operation co-optimization model is formulated in a compact form as

$$\text{(P1)} \quad \min_{\boldsymbol{x_t}} \quad \sum_{t\in\mathcal{T}} \boldsymbol{c_t}^{\mathrm{T}} \boldsymbol{x_t} \tag{13}$$

$$\text{s.t.} \quad \boldsymbol{B_t x_t} \leq \boldsymbol{h_t}, \forall t \in \mathcal{T}, \tag{14}$$

where $\boldsymbol{x_t}$ denotes the vector of decision variables. Matrix $\boldsymbol{B_t}$ and vectors $\boldsymbol{c_t}, \boldsymbol{h_t}$ are the corresponding coefficients.

B. Variable Timescale Model

In the proposed variable timescale model, the scheduling of flexible resources is focused on critical time periods during ramp events occurring. In this way, the binary decisions (i.e, MESS mobility) could be made in the high-resolution time periods. It helps unlock flexibility while maintaining an efficient model size. Fig. 3 shows the diagram of timescale adjustment. The adjusted time set $\tilde{\mathcal{T}}$ can be obtained based on ramp events. Specifically, the timescale during ramp events occurring can be further refined. Then, by replacing the original time set $\mathcal{T}$ in (P1) with the adjusted time set $\tilde{\mathcal{T}}$, the variable timescale model can be formulated as

$$\text{(P2)} \quad \min_{\boldsymbol{x_t}} \quad \sum_{t\in\tilde{\mathcal{T}}} \tilde{\boldsymbol{c}}_{\boldsymbol{t}}^{\mathrm{T}} \boldsymbol{x_t} \tag{15}$$

$$\text{s.t.} \quad \tilde{\boldsymbol{B}}_{\boldsymbol{t}} \boldsymbol{x_t} \leq \tilde{\boldsymbol{h}}_{\boldsymbol{t}}, \forall t \in \tilde{\mathcal{T}}. \tag{16}$$

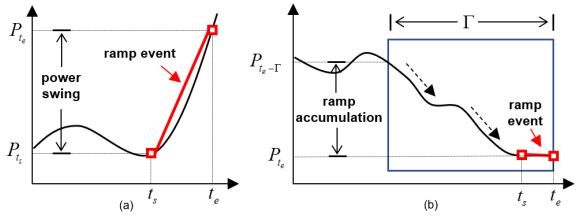

Fig. 4. Diagram of two net load ramp events that satisfy the power swing threshold (a) and ramp accumulation threshold (b), respectively.

III. Critical Ramp Event Detection

This section proposes a novel critical ramp event detection algorithm for identifying ramp events. The complete algorithm integrates trend fitting, ramp rules and ramp events detection.

A. Trend Fitting

The net load time series contains many tiny smooth segments that are outside of our interest. Trend fitting is capable of eliminating these segments and revealing the trends in time series. Hence, this paper uses a trend fitting algorithm called critical aperture filtering [32] as a preprocessing step, which is proposed for efficient data compression in a data management system formerly. In this algorithm, a series of data points are evaluated one after the other in view of a critical aperture, which is the upper and lower slopes related to a previous archived data point. If the point following the previous archived point falls within the critical aperture, it will be discarded. Otherwise, it will be archived.

B. Ramp Rules

Generally, a ramp represents a significant increase or decrease in load power within a limited time span. The following rule [21] is usually used to determine whether an interval of the load time series is in fact a ramp event.

$$R_1(t_s, t_e) = \mathbf{1}_{\{|P_{t_e} - P_{t_s}| \geq \mathcal{Z}_m\}}, t_e - t_s \leq \bar{t}, \tag{17}$$

where t_s and t_e denote the start and end time of time series, respectively. $R(t_s, t_e)$ is 1 if the event satisfies the threshold, and 0 otherwise. P_t is the power of time series at time t. $\bar{t}$ is the maximum time span of each ramp event. $\mathcal{Z}_m$ represent the threshold of power swing. Equation (17) specifies the power swing rule which checks whether the load power has changed by a specified amount in a given time span.

On the other hand, because of the limited SOC, excessive accumulation of continuous ramp-up/-down events poses a challenge to energy storage systems. It could force MESS to move its location during the load duration time. For example, overcharge could happen after several continuous ramp-up events of PV. If the voltage of the node MESS connected is at a high level, MESS then needs to move to other nodes with higher voltage safety margins for releasing the energy. Thus, we develop a concise rule to determine whether an interval has accumulated excessive continuous ramp-up/-down events:

$$R_2(t_s, t_e) = \mathbf{1}_{\{|P_{t_e} - P_{t_e-\Gamma}| \geq \mathcal{Z}_c\}}, t_e - t_s \leq \bar{t}, \tag{18}$$

Algorithm 1 Ramp Event Detection Algorithm

Input: P obtained by trend fitting of forecast net load
Output: Set of mutually independent ramp events RE^*
$k \leftarrow 1$, $RE_1 \leftarrow \emptyset$
for $t_s = 1 \rightarrow \text{length}(P) - 1$ **do**
  for $t_e = t_s + 1 \rightarrow \min\{t_s + \bar{t}, \text{length}(P)\}$ **do**
    if $R_1(t_s, t_e) == 1$ or $R_2(t_s, t_e) == 1$ **then**
      $s_k \leftarrow t_s$, $e_k \leftarrow t_e$, $m_k \leftarrow |P_{t_e} - P_{t_s}|$
      $c_k \leftarrow |P_{t_e} - P_{t_e - \Gamma}|$, $RE_k \leftarrow (s_k, e_k, m_k, c_k)$
      $k \leftarrow k + 1$
    end if
  end for
end for
$K \leftarrow k - 1$, $k \leftarrow 1$, $RE_1^* \leftarrow RE_1$
for $k' = 2 \rightarrow K$ **do**
  if $e_k^* > s_{k'}$ **then**
    if $f(RE_k^*) < f(RE_{k'})$ **then**
      $RE_k^* \leftarrow \emptyset$, $RE_k^* \leftarrow RE_{k'}$
    end if
  else
    $k \leftarrow k + 1$, $RE_k^* \leftarrow RE_{k'}$
  end if
end for

where Γ is a memory factor. $\mathcal{Z}_c$ represents the threshold of ramp accumulation. Equation (18) defines a ramp accumulation rule. Fig. 4 shows the diagram of the net load ramp events that satisfy the two ramp rules.

C. Ramp Events Detection

The ramp detection is performed based on the rules outlined in (17)-(18) using Algorithm 1. Algorithm 1 traverses the input time series P and identifies all ramp events RE that satisfy the ramp rules first. Then it extracts mutually independent events RE^* from the overlapping events in RE based on a score function. For a given ramp event RE_k, the corresponding score value is attained as follows:

$$f(RE_k) = \rho_1|m_k| + \rho_2|e_k - s_k| + \rho_3|c_k|, \tag{19}$$

where m_k, e_k, s_k and c_k denote the power swing, end time, start time and ramp accumulation of RE_k, respectively.

As a side note, the ramp event detection is performed using the data of forecast net load. The forecast net load can be obtained based on the forecast load curve, the per-unit forecast PV curve, and the proportion of total PV capacity to total load ν. The uncertainty of forecast error is accommodated by the recourse actions, which will be explained in the following section. The effectiveness of this method is adequately verified in the case study. It is worth mentioning that uncertainty can also be considered in the detection algorithm to further enhance the accuracy of the variable timescale model by replacing $R_1(t_s, t_e)$ with $R_1^*(t_s, t_e)$:

$$R_1^*(t_s, t_e) = \mathbf{1}_{\{\max\{\overline{P}_{t_e} - \underline{P}_{t_s}, \overline{P}_{t_s} - \underline{P}_{t_e}\} \geq \mathcal{Z}_m\}}, t_e - t_s \leq \bar{t},$$

where $\overline{P}_t, \underline{P}_t$ denote the upper and lower bounds of the confidence interval for the forecast net load at time t, respectively.

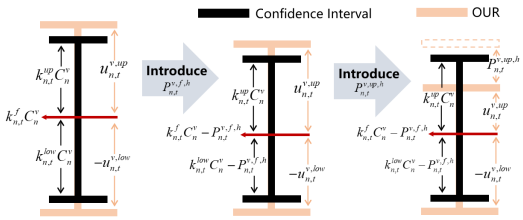

Fig. 5. Comparison of the PV optimal uncertainty range (OUR), forecast confidence interval and curtailment.

IV. Multistage Model With Variable Uncertainty Set

In this section, we present the uncertainty model and formulate a multistage model with variable uncertainty set.

A. Uncertainty Modeling

In this study, the deviations from PV generation forecast and load forecast are considered as uncertainty. Uncertainty set is a key factor in multistage models, and is usually formulated as a box set with certain boundary [23], [24], [26]. However, PV installation capacity, load shedding and PV curtailment are decision variables in this work. Hence, the uncertainty set is not a constant anymore. We formulate the uncertainty set with variable bounds as

$$\mathcal{U}_t = \left\{ \begin{array}{l} \mathcal{U}_{m,t}^d = \{\epsilon_{m,t}^d | u_{m,t}^{d,low} \leq \epsilon_{m,t}^d \leq u_{m,t}^{d,up}\}, \forall m \in \mathcal{M}, \\ \mathcal{U}_{n,t}^v = \{\epsilon_{n,t}^v | u_{n,t}^{v,low} \leq \epsilon_{n,t}^v \leq u_{n,t}^{v,up}\}, \forall n \in \mathcal{N}, \\ u_{m,t}^{d,low} \leq 0, u_{n,t}^{v,low} \leq 0, u_{m,t}^{d,up} \geq 0, u_{n,t}^{v,up} \geq 0. \end{array} \right\}, \\ \forall t \in \tilde{\mathcal{T}}, \tag{20}$$

which denotes the optimal range of uncertainty that the flexibility is capable of accommodating. $\mathcal{U}_t$ can be called Optimal Uncertainty Range (OUR). It is related to forecast confidence interval, forecast value, PV curtailment, load shedding and PV installation capacity. We formulate constraints as follows

$$P_{m,t}^{d,low} \leq -u_{m,t}^{d,low} + P_{m,t}^{d,f,h} \leq P_{m,t}^{d,f}, \forall t \in \tilde{\mathcal{T}}, \forall m \in \mathcal{M}, \tag{21}$$

$$P_{m,t}^{d,up} \leq u_{m,t}^{d,up} + P_{m,t}^{d,up,h}, \forall t \in \tilde{\mathcal{T}}, \forall m \in \mathcal{M}, \tag{22}$$

$$k_{n,t}^{low} C_n^v \leq -u_{n,t}^{v,low} + P_{n,t}^{v,f,h} \leq k_{n,t}^f C_n^v, \forall t \in \tilde{\mathcal{T}}, \forall n \in \mathcal{N}, \tag{23}$$

$$k_{n,t}^{up} C_n^v \leq u_{n,t}^{v,up} + P_{n,t}^{v,up,h} \leq C_n^v - k_{n,t}^f C_n^v + P_{n,t}^{v,f,h}, \\ \forall t \in \tilde{\mathcal{T}}, \forall n \in \mathcal{N}, \tag{24}$$

where $P_{m,t}^{d,f,h}, P_{n,t}^{v,f,h}$ denote the load shedding and PV curtailment in the forecast scenario, respectively. $P_{m,t}^{d,up,h}, P_{n,t}^{v,up,h}$ denote the load shedding and PV curtailment of upward flexibility (allowed upward deviation of uncertainty $u_{m,t}^{d,up}, u_{n,t}^{v,up}$), respectively. The total load shedding and PV curtailment can be denoted by $P_{m,t}^{d,h} = P_{m,t}^{d,f,h} + P_{m,t}^{d,up,h}$ and $P_{n,t}^{v,h} = P_{n,t}^{v,f,h} + P_{n,t}^{v,up,h}$, respectively. Constraints (21)-(24) ensure that uncertainty in the confidence interval can always be accommodated in OUR if there is no PV curtailment or load shedding. For illustrative purposes, we present the relationship between PV OUR, confidence interval and curtailment in Fig. 5.

B. Multistage Optimization Model

When uncertainty is materialized, it has to be accommodated by recourse actions, which are formulated as

$$[\hat{P}_t^b, \hat{Q}_t^b, \hat{P}_{c,l,t}^{s,c}, \hat{P}_{c,l,t}^{s,d}, \hat{V}_{i,t}, \hat{P}_{q,t}, \hat{Q}_{q,t}] = [P_t^b, Q_t^b, P_{c,l,t}^{s,c}, P_{c,l,t}^{s,d}, V_{i,t}, P_{q,t}, Q_{q,t}] + \boldsymbol{y_t}(\boldsymbol{\epsilon_{[t]}}), \forall \boldsymbol{\epsilon_t} \in \mathcal{U}_t, i \in \mathcal{I}, \forall c \in \mathcal{C}, \forall l \in \mathcal{L}, q \in \mathcal{Q}, \forall t \in \tilde{\mathcal{T}}, \quad (25)$$

where $\boldsymbol{\epsilon_{[t]}}$ is the uncertainty vector at stage t and $\boldsymbol{\epsilon_{[t]}} = \{\boldsymbol{\epsilon_1}, \boldsymbol{\epsilon_2}, ..., \boldsymbol{\epsilon_t}\}$. $\boldsymbol{y_t}(\boldsymbol{\epsilon_{[t]}})$ is the re-dispatch policy that maps uncertainty to recourse actions. The recourse actions at stage t depend on the realizations of uncertainty up to stage t. According to [33], *nonanticipativity* refers to that the current re-dispatch decision can only be made based on the current and previous information available, and is independent of unknown uncertainty realizations of the future. Thus, the recourse actions (25) guarantee the nonanticipativity. Moreover, to guarantee that solutions are feasible for any uncertainty realization within the uncertainty set, which is called *robustness*, they are forced to satisfy constraints (4)-(12).

With aforementioned equations, a multistage model with variable uncertainty set is proposed. For notation simplicity, the compact form of the model is rewritten as

$$\text{(P3)} \min_{\boldsymbol{x_t}, \boldsymbol{u_t}, \boldsymbol{y_t}(.)} \quad \sum_{t \in \tilde{\mathcal{T}}} \tilde{\boldsymbol{c}}_{\boldsymbol{t}}{}^{\mathrm{T}} \boldsymbol{x_t} \quad (26)$$

$$\text{s.t.} \quad \boldsymbol{A_t x_t} + \boldsymbol{E_t u_t} \leq \boldsymbol{b_t}, \forall t \in \tilde{\mathcal{T}}, \quad (27)$$

$$\sum_{\tau=1}^{t} \left[\boldsymbol{K_\tau x_\tau} + \boldsymbol{M_\tau y_\tau}(\boldsymbol{\epsilon_{[\tau]}})\right] + \boldsymbol{L_t \epsilon_t} \leq \boldsymbol{d_t}, \forall \boldsymbol{\epsilon_t} \in \mathcal{U}_t, \forall t \in \tilde{\mathcal{T}}, \quad (28)$$

where $\boldsymbol{u_t}$ denotes the bound of uncertainty set. Equation (27) represents constraints (1)-(3) and (21)-(24). The re-dispatch constraints (4)-(12) and (25) are rewritten in (28). As a side note, the MESS mobility is optimally determined, and MESS mobility does not take recourse action in this work. That is mainly because the recourse action of mobility poses significant computational challenges to the multistage model. Hence, some optimality is sacrificed to guarantee the computational tractability.

V. Hybrid Solution Approach

(P3) is intractable due to the infinite constraints (28) and variable uncertainty set $\mathcal{U}_t$. To overcome these challenges, we propose a novel hybrid solution approach, including SAP-based model reformulation and hybrid acceleration strategy.

A. Surrogate Affine Policy with Multistage Model

Affine policy is commonly used to approximate the re-dispatch decisions $\boldsymbol{y_t}(\boldsymbol{\epsilon_{[t]}})$ as affine functions of uncertainty to make the multistage problem tractable [9], [23], [24]. Let $\boldsymbol{G_t}$ denotes the affine matrix. $\boldsymbol{y_t}(\boldsymbol{\epsilon_{[t]}})$ is then described as

$$\boldsymbol{y_t}\left(\boldsymbol{\epsilon_{[t]}}\right) = \boldsymbol{G_t \epsilon_t}, \forall t \in \tilde{\mathcal{T}}, \forall \boldsymbol{\epsilon_t} \in \mathcal{U}_t. \quad (29)$$

However, the traditional linear affine policy is intractable to solve problem (P3) due to the variable uncertainty set [27].

Algorithm 2 Hybrid Acceleration Strategy

```
Screen inactive security constraints with (C)
Reformulate power balance constraints into (47)-(48)
Reformulate MESS output constraints into (50)
Reformulate SOC constraints into (51)-(53)
Initialize D_f for all f with a set of initial extreme points
while g_f(x', u', Ĝ', δ) > 0, ∃δ ∈ Û, ∃f ∈ {1, ...F} do
    (x', u', Ĝ') ← optimal solution of (P5)
    for f ∈ {1, ..., F} do
        δ_f ← argmax_{δ∈Û} g_f(x', u', Ĝ', δ)
        If g_f(x', u', Ĝ', δ_f) > 0 let D_f ← D_f ∪ {δ_f}
    end for
end while
Output the optimal solution (x', u', Ĝ')
```

The duality-based approach or scenario generation method cannot solve it directly, which are often used to handle the two-stage/multistage robust model with a constant uncertainty set. Inspired by [27], we utilize SAP to recast the problem into the multistage model with a constant uncertainty set. First, we introduce the new surrogate uncertainty set

$$\hat{\mathcal{U}}_t = \{\boldsymbol{\delta_t} | \boldsymbol{0} \leq \boldsymbol{\delta_t} \leq \boldsymbol{1}\}, \forall t \in \tilde{\mathcal{T}}, \quad (30)$$

and surrogate affine policy

$$\hat{\boldsymbol{G}}_{\boldsymbol{t}} = \boldsymbol{G_t}[\boldsymbol{U_t^-}, \boldsymbol{U_t^+}], \forall t \in \tilde{\mathcal{T}}, \quad (31)$$

where $\boldsymbol{U_t^-} = \mathrm{diag}(\boldsymbol{u_t^{low}})$, $\boldsymbol{U_t^+} = \mathrm{diag}(\boldsymbol{u_t^{up}})$. $\boldsymbol{u_t^{low}}$ and $\boldsymbol{u_t^{up}}$ are the lower and upper bound of uncertainty set, respectively. Then, the uncertainty and re-dispatch policy can be recast as

$$\boldsymbol{\epsilon_t} = [\boldsymbol{U_t^-}, \boldsymbol{U_t^+}][\boldsymbol{\delta_t}, \boldsymbol{1} - \boldsymbol{\delta_t}]^{\mathrm{T}}, \boldsymbol{G_t \epsilon_t} = \hat{\boldsymbol{G}}_{\boldsymbol{t}}[\boldsymbol{\delta_t}, \boldsymbol{1} - \boldsymbol{\delta_t}]^{\mathrm{T}}, \forall t \in \tilde{\mathcal{T}}. \quad (32)$$

Next, we substitute (29) and (32) into (28). Then, equation (28) is recast as

$$\sum_{\tau=1}^{t} \left\{\boldsymbol{K_\tau x_\tau} + \boldsymbol{M_\tau} \hat{\boldsymbol{G}}_{\boldsymbol{\tau}}[\boldsymbol{\delta_\tau}, \boldsymbol{1} - \boldsymbol{\delta_\tau}]^{\mathrm{T}}\right\} + \boldsymbol{L_t}[\boldsymbol{U_t^-}, \boldsymbol{U_t^+}][\boldsymbol{\delta_t}, \boldsymbol{1} - \boldsymbol{\delta_t}]^{\mathrm{T}} \leq \boldsymbol{d_t}, \forall \boldsymbol{\delta_t} \in \hat{\mathcal{U}}_t, \forall t \in \tilde{\mathcal{T}}. \quad (33)$$

Finally, the SAP-based multistage model with a constant uncertainty set is formulated as

$$\text{(P4)} \min_{\boldsymbol{x_t}, \boldsymbol{u_t}, \hat{\boldsymbol{G}}_{\boldsymbol{t}}} \quad \sum_{t \in \tilde{\mathcal{T}}} \tilde{\boldsymbol{c}}_{\boldsymbol{t}}{}^{\mathrm{T}} \boldsymbol{x_t} \quad (34)$$

$$\text{s.t.} \quad (27), (33). \quad (35)$$

B. Hybrid Acceleration Strategy

The SAP-based model is typically solved by the duality-based approach [27], [28], which recasts (33) by its dual program with additional dual variables and constraints. However, the additional dual variables and constraints increase significantly with the number of buses, loads and PVs, leading to a prohibitively high computational burden. Inspired by the idea from [24], we propose a hybrid acceleration strategy to overcome the scalability issue of solving (P4), as presented in Algorithm 2.

1) Security Constraint Screening: In the dual-based solution approach, overwhelming security constraints (11)-(12) may result in scalability issues in large-scale systems. Inspired by [34], we formulate a mixed integer quadratically constrained program model to screen inactive security constraints. Take the constraint of voltage upper limit as an example, the basic idea is to check whether the largest possible nodal voltage $V_{j,t}$ can exceed its upper limit. It is formulated as:

$$\text{(C)} \quad V_{j,t} =: \max \sum_{i\in\mathcal{I}} \left(\Omega_{j,i}^{V,P} P_{i,t}^{\text{inj}} + \Omega_{j,i}^{V,Q} Q_{i,t}^{\text{inj}}\right) \tag{36}$$

$$\text{s.t.} P_{i,t}^{\text{inj}} = \sum_{l\in\mathcal{L}} \sum_{c\in\mathcal{G}(i)} P_{c,l,t}^{s} + \sum_{n\in\mathcal{F}(i)} P_{n,t}^{v} - \sum_{m\in\mathcal{P}(i)} P_{m,t}^{d}, i \in \mathcal{I}, \tag{37}$$

$$Q_{i,t}^{\text{inj}} = - \sum_{m\in\mathcal{P}(i)} Q_{m,t}^{d}, \forall i \in \mathcal{I}, \tag{38}$$

$$\underline{V} \le \sum_{i\in\mathcal{I}} \left(\Omega_{j',i}^{V,P} P_{i,t}^{\text{inj}} + \Omega_{j',i}^{V,Q} Q_{i,t}^{\text{inj}}\right) \le \bar{V}, \forall j' \in \mathcal{I}\backslash j, \tag{39}$$

$$\left(\sum_{i\in\mathcal{I}} \Omega_{q,i}^{S,P} P_{i,t}^{\text{inj}}\right)^2 + \left(\sum_{i\in\mathcal{I}} \Omega_{q,i}^{S,Q} Q_{i,t}^{\text{inj}}\right)^2 \le \bar{S}_q^2, q \in \mathcal{Q}, \tag{40}$$

$$P_{m,t}^{d,f} - P_{m,t}^{d,low} \le P_{m,t}^{d} \le P_{m,t}^{d,f} + P_{m,t}^{d,up}, \forall m \in \mathcal{M}, \tag{41}$$

$$Q_{m,t}^{d,f} - Q_{m,t}^{d,low} \le Q_{m,t}^{d} \le Q_{m,t}^{d,f} + Q_{m,t}^{d,up}, \forall m \in \mathcal{M}, \tag{42}$$

$$(k_{n,t}^{f} - k_{n,t}^{low}) C_n^v \le P_{n,t}^{v} \le (k_{n,t}^{f} + k_{n,t}^{up}) C_n^v, \forall n \in \mathcal{N}, \tag{43}$$

$$-\eta_l^c \lambda_{c,l,t} C_l^s \le P_{c,l,t}^{s} \le \eta_l^d \lambda_{c,l,t} C_l^s, \forall c \in \mathcal{C}, \forall l \in \mathcal{L}, \tag{44}$$

$$\sum_{c\in\mathcal{C}} \lambda_{c,l,t} \le 1, \forall l \in \mathcal{L}, \tag{45}$$

where $\mathcal{G}(i), \mathcal{F}(i), \mathcal{P}(i)$ denote the sets of MESS candidate location, PV and load located at bus i, respectively. $P_{c,l,t}^{s}$ is the net discharging power of MESS. $Q_{m,t}^{d,f}, Q_{m,t}^{d,up}, Q_{m,t}^{d,low}$ denote the forecast value, upper and lower bound for the confidence interval of load's reactive power, respectively. Power flows and voltage magnitudes are described as images of nodal power injections, and $\Omega_{j,i}^{V,P}, \Omega_{j,i}^{V,Q}, \Omega_{q,i}^{S,P}, \Omega_{q,i}^{S,Q}$ denote the coefficients of these images, which can be obtained in [9].

Problem (C) is to find the largest possible $V_{j,t}$ respecting all other security and physics constraints. The voltage upper constraint of bus j at time t can be ignored if $V_{j,t} \le \bar{V}$. For simplicity, the screening formulations of other security constraints are not presented, which is similar. Note that (C) can be solved in parallel to improve the solution time.

2) Reformulation of Power Balance Constraints: The infinite constraints of power balance can be written as

$$\boldsymbol{J_t}[\hat{\boldsymbol{G}}_{\boldsymbol{t}}', \hat{\boldsymbol{G}}_{\boldsymbol{t}}''][\boldsymbol{\delta_t}, \boldsymbol{1} - \boldsymbol{\delta_t}]^{\mathrm{T}} + \boldsymbol{H_t}[\boldsymbol{U_t^-}, \boldsymbol{U_t^+}][\boldsymbol{\delta_t}, \boldsymbol{1} - \boldsymbol{\delta_t}]^{\mathrm{T}} + \boldsymbol{V_t x_t} = \boldsymbol{q_t}, \forall t \in \tilde{\mathcal{T}}, \forall \boldsymbol{\delta_t} \in \hat{\mathcal{U}}_t, \tag{46}$$

where $\hat{\boldsymbol{G}}_{\boldsymbol{t}}', \hat{\boldsymbol{G}}_{\boldsymbol{t}}''$ denote the decision variables of the SAP $\hat{\boldsymbol{G}}_{\boldsymbol{t}}$. It is equivalent to the following equations

$$\boldsymbol{J_t}\hat{\boldsymbol{G}}_{\boldsymbol{t}}'' + \boldsymbol{H_t U_t^+} + \boldsymbol{V_t x_t} = \boldsymbol{q_t}, \forall t \in \tilde{\mathcal{T}}, \tag{47}$$

$$\boldsymbol{J_t}\hat{\boldsymbol{G}}_{\boldsymbol{t}}' - \boldsymbol{J_t}\hat{\boldsymbol{G}}_{\boldsymbol{t}}'' + \boldsymbol{H_t U_t^-} - \boldsymbol{H_t U_t^+} = \boldsymbol{0}, \forall t \in \tilde{\mathcal{T}}. \tag{48}$$

3) Reformulation of MESS Output Bounds: When the uncertainty is materialized, MESS adjusts its output as recourse action. We employ the simplified SAP $\hat{\boldsymbol{G}}_{\boldsymbol{t}}^{\boldsymbol{s}}$ associated with an aggregation of uncertainty to mitigate the scalability issue:

$$\begin{aligned}[\hat{\boldsymbol{P}}_{\boldsymbol{t}}^{\boldsymbol{s,d}}, \hat{\boldsymbol{P}}_{\boldsymbol{t}}^{\boldsymbol{s,c}}] &= [\boldsymbol{P}_{\boldsymbol{t}}^{\boldsymbol{s,d}}, \boldsymbol{P}_{\boldsymbol{t}}^{\boldsymbol{s,c}}] + \hat{\boldsymbol{G}}_{\boldsymbol{t}}^{\boldsymbol{s}}[\tilde{\delta}_t^v, \tilde{\delta}_t^d, 1-\tilde{\delta}_t^v, 1-\tilde{\delta}_t^d]^{\mathrm{T}} \\ &= [\boldsymbol{P}_{\boldsymbol{t}}^{\boldsymbol{s,d}}, \boldsymbol{P}_{\boldsymbol{t}}^{\boldsymbol{s,c}}] + \hat{\boldsymbol{G}}_{\boldsymbol{t}}^{\boldsymbol{s}'}[\tilde{\delta}_t^v, \tilde{\delta}_t^d]^{\mathrm{T}} + \hat{\boldsymbol{G}}_{\boldsymbol{t}}^{\boldsymbol{s}''}, \\ &\forall t \in \tilde{\mathcal{T}}, \forall \tilde{\delta}_t^v \in [0,1], \forall \tilde{\delta}_t^d \in [0,1], \end{aligned} \tag{49}$$

where $\tilde{\delta}_t^v = \sum_{n\in\mathcal{N}} \delta_{n,t}^v / N_n$, $\tilde{\delta}_t^d = \sum_{m\in\mathcal{M}} \delta_{m,t}^d / N_m$. $\hat{\boldsymbol{G}}_{\boldsymbol{t}}^{\boldsymbol{s}'}, \hat{\boldsymbol{G}}_{\boldsymbol{t}}^{\boldsymbol{s}''}$ denote the decision variables of the simplified SAP. The re-dispatch of MESS output is a function of the system-level power of PV and load. A similar strategy has been widely used in the multistage models [23]–[25] to overcome the computational difficulties from the full affine policy. As shown in section VI-A, this simplified policy performs surprisingly well for (P4).

Under the simplified SAP, the infinite constraints of MESS output are recasted as:

$$\boldsymbol{0} \le [\boldsymbol{P}_{\boldsymbol{t}}^{\boldsymbol{s,d}}, \boldsymbol{P}_{\boldsymbol{t}}^{\boldsymbol{s,c}}] + \hat{\boldsymbol{G}}_{\boldsymbol{t}}^{\boldsymbol{s}'}[\tilde{\delta}_t^v, \tilde{\delta}_t^d]^{\mathrm{T}} + \hat{\boldsymbol{G}}_{\boldsymbol{t}}^{\boldsymbol{s}''} \le \boldsymbol{R_t x_t}, \forall t \in \tilde{\mathcal{T}}, \forall \tilde{\delta}_t^v \in \{0,1\}, \forall \tilde{\delta}_t^d \in \{0,1\}. \tag{50}$$

The proof is trivial. The MESS output is at its maximum or minimum if and only if $\tilde{\delta}_t^v, \tilde{\delta}_t^d$ take the vertex values.

4) Duality-based Reformulation of SOC Constraints: Take the infinite constraints of SOC upper limit of l-th MESS at time t as an example, it can be written as

$$0 \ge \left\{ \begin{array}{ll} \max\limits_{\tilde{\delta}_\tau^v, \tilde{\delta}_\tau^d} & \sum\limits_{\tau=1}^{t} \left\{ \boldsymbol{s_\tau^{\mathrm{T}} x_\tau} + \boldsymbol{w_\tau^{\mathrm{T}}} \hat{\boldsymbol{G}}_{\boldsymbol{\tau}}^{\boldsymbol{s}'} [\tilde{\delta}_\tau^v, \tilde{\delta}_\tau^d]^{\mathrm{T}} + \boldsymbol{w_\tau^{\mathrm{T}}} \hat{\boldsymbol{G}}_{\boldsymbol{\tau}}^{\boldsymbol{s}''} \right\} \\ \text{s.t.} & 0 \le \tilde{\delta}_\tau^v \le 1, 0 \le \tilde{\delta}_\tau^d \le 1, \forall \tau \in \{1,2,...,t\} \end{array} \right\}$$

Based on the duality theory [35], it can be recast as

$$\sum_{\tau=1}^{t} \left(\boldsymbol{s_\tau^{\mathrm{T}} x_\tau} + \boldsymbol{w_\tau^{\mathrm{T}}} \hat{\boldsymbol{G}}_{\boldsymbol{\tau}}^{\boldsymbol{s}''} \right) + [\boldsymbol{\pi_{t,1}}, \boldsymbol{\pi_{t,2}}, ..., \boldsymbol{\pi_{t,t}}] \cdot \boldsymbol{1} \le 0, \tag{51}$$

$$\boldsymbol{w_\tau^{\mathrm{T}}} \hat{\boldsymbol{G}}_{\boldsymbol{\tau}}^{\boldsymbol{s}'} \le \boldsymbol{\pi_{t,\tau}}, \forall \tau \in \{1,2,...,t\}, \tag{52}$$

$$\boldsymbol{\pi_{t,\tau}} \ge \boldsymbol{0}, \forall \tau \in \{1,2,...,t\}. \tag{53}$$

5) Scenario Generation: In this work, we will handle the security constraints through Scenario Generation (SG) approach. The master problem in the SG algorithm can be written as

$$\text{(P5)} \min_{\boldsymbol{x_t}, \boldsymbol{u_t}, \hat{\boldsymbol{G}}_{\boldsymbol{t}}, \boldsymbol{\pi_{t,\tau}}} \sum_{t\in\tilde{\mathcal{T}}} \tilde{\boldsymbol{c}}_{\boldsymbol{t}}^{\mathrm{T}} \boldsymbol{x_t} \tag{54}$$

$$\text{s.t.} \quad (27), (47)\text{-}(48), (50)\text{-}(53), \tag{55}$$

$$g_f(\boldsymbol{x}, \boldsymbol{u}, \hat{\boldsymbol{G}}, \boldsymbol{\delta}) \le 0, \forall \boldsymbol{\delta} \in D_f, \forall f \in \{1,..,F\}, \tag{56}$$

where D_f denotes the set of extreme points identified from the SG algorithm for security constraint f. $\{1,...,F\}$ is the set of possibly-binding security constraints obtained by the proposed screening method. $g_f(\boldsymbol{x}, \boldsymbol{u}, \hat{\boldsymbol{G}}, \boldsymbol{\delta})$ is f-th security constraint. The SG solves the master problem (P5), and checks if the f-th constraint is violated by the solution, and if so, the associated scenario is added to D_f. To reduce the number of (P5) solved in the algorithm, we start with an initial set of extreme points (i.e., the scenarios with the minimum net load and maximum net load).

TABLE I
MAJOR TECHNO-ECONOMICAL PARAMETERS

PV	R^v = \$534/kW, y^v = 25 yr
Feeder	$\underline{V}$ = 0.95, $\bar{V}$= 1.05, ρ^{b+} = \$0.25/kWh
MESS	α^s = 0.9, R^s = \$519/kWh, y^s = 10 yr $\eta^d = \eta^c = 0.5$, $\mu^c = \mu^d = 1$, ρ^o = \$5/h

TABLE II
PARAMETERS OF RAMPING EVENT DETECTION

Parameter	Value	Parameter	Value
$\mathcal{Z}_m$, $\mathcal{Z}_c$	0.2 p.u., 0.4 p.u.	$\mathcal{W}$	0.005 p.u.
$\bar{t}$, Γ, ν	4 h, 6 h, 1.4	ρ_1, ρ_2 ,ρ_3	1, 0, 5

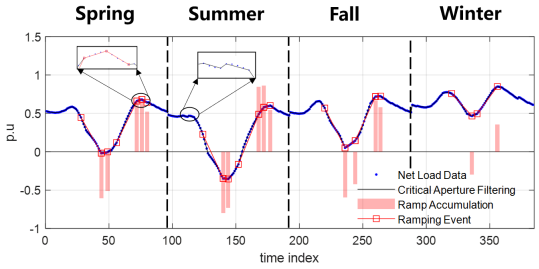

Fig. 6. Seasonal net load time series with critical aperture filtering, detected ramp events and ramp accumulation. Critical aperture filtering reduces the original time series from 384 samples to 98 samples. 16 ramp events are detected and 14 of them are over-accumulation events.

VI. CASE STUDY

Numerical tests are carried out with the modified IEEE 13-bus system [36], 141-bus system [28] and 906-bus system [37]. We use four seasonal typical days for the planning. Typical load and PV profiles for each season are from [38]. In the planning stage, the uncertainty bounds for PV and load are set to 0.2 p.u. In the scheduling stage, the uncertainty bounds expand as the prediction time scale increases, ranging from 0.05 p.u. to 0.2 p.u.. PVs are assumed to operate at the unity power, and the load's power factor is 0.85. The major techno-economical parameters are presented in Table I. The cost of PV curtailment and load shedding is set to \$5000/MWh. The simulations are executed using Matlab 2021b and Gurobi 9.5.

The proposed critical ramp event detection method is applied to seasonal net load time series. The detection parameters are presented in Table II. Fig. 6 shows the seasonal net load time series with critical aperture filtering, detected ramp events and ramp accumulation. The net load reaches valley value at 11:45 in summer. Critical aperture filtering reduces the net load time series from 384 samples to 98 samples. It produces a good fit with low approximation error. The method detects 16 ramp events after filtering. Note that some of them are over-accumulation ramp events with short duration. For example, the 2nd ramp event occurs from 10:45 to 12:00 in spring, which has a power swing of 0.02 p.u. and ramp accumulation of 0.51 p.u.. Although these events are inconspicuous, SOC of MESS is very likely to hit the security bound during these periods, necessitating movement. It will be discussed in section VI-A.

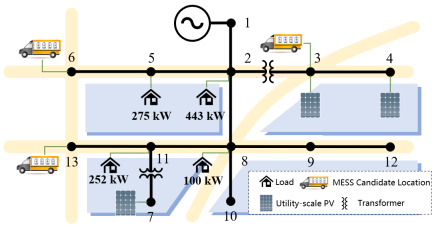

Fig. 7. Single-line diagram of the modified IEEE 13-bus system coupled with a transportation network.

TABLE III
PLANNING RESULTS OF IEEE 13-BUS SYSTEM WITH ONE MESS

	Cost (\$)	MESS Cap. (kWh)	PV Cap. (kW) Node 3	Node 4	Node 7	LCN (10^3)	LVN (10^3)	LST (s)
Case 1	15134	560	626	0	71	9.4	6.7	6
Case 2	**15067**	642	659	0	73	19.1	14.0	14
Case 3	**15067**	642	659	0	73	28.9	22.5	26

TABLE IV
PLANNING RESULTS OF IEEE 13-BUS SYSTEM WITH TWO MESSS

	Cost (\$)	MESS Cap. (kWh) No.1	No.2	PV Cap. (kW) Node 3	Node 4	Node 7	LCN (10^3)	LVN (10^3)	LST (s)
Case 1	15131	545	26	622	0	78	16.8	12.1	88
Case 2	**15058**	510	254	696	0	66	35.1	26.2	616
Case 3	**15058**	510	254	696	0	66	54.7	42.7	1473

A. 13-bus Distribution System

Fig. 7 illustrates the single-line diagram of the modified IEEE 13-bus system with a nominal voltage of 2.40 kV. The feeder includes 4 load nodes with the peak being 1.07 MW and 0.66 MVar. The apparent power capacity of the branch is 2 MVA. Utility-scale PVs are to be installed at node 3, 4, 7. There are 3 MESS candidate locations, where MESSs can be connected to the power system. The initial and terminal location are node 13. The travel time between each MESS candidate location is 30 min. The initial SOC is set as 50%. The voltage ratios of the two transformers are set to 1:1.06 and 1:1.07, respectively.

1) Comparison with Fixed Timescale Model: The following cases are performed to validate the effectiveness of the proposed ramping-based variable-timescale model in selectively refining the time resolution:

- Case 1: Optimization with a fixed timescale of 1 h.
- Case 2: Optimization with a variable timescale between 0.5 h and 1 h, which is determined based on ramp events.
- Case 3: Optimization with a fixed timescale of 0.5 h.

In Case 1, the time resolution of 1 h is utilized, which is commonly used in both planning and scheduling models [6], [7], [10], [11]. In Case 2, the time resolution is selectively refined from 1 h to 0.5 h during ramp events. In Case 3, the time resolution of 0.5 h [13] is used as a benchmark to represent the fully fine resolution. Case 3 is designed to obtain the most exact planning results among the three cases due to its finest time resolution. It is used to evaluate the results obtained from the other two cases. In each case, the forecast values of load and PV for each time period are calculated by averaging the 15-minute forecast values to ensure a fair comparison.

Firstly, we perform the proposed model for planning with one MESS, as shown in Table III. "Cost" represents the planning and operation cost of four seasonal typical days. "MESS

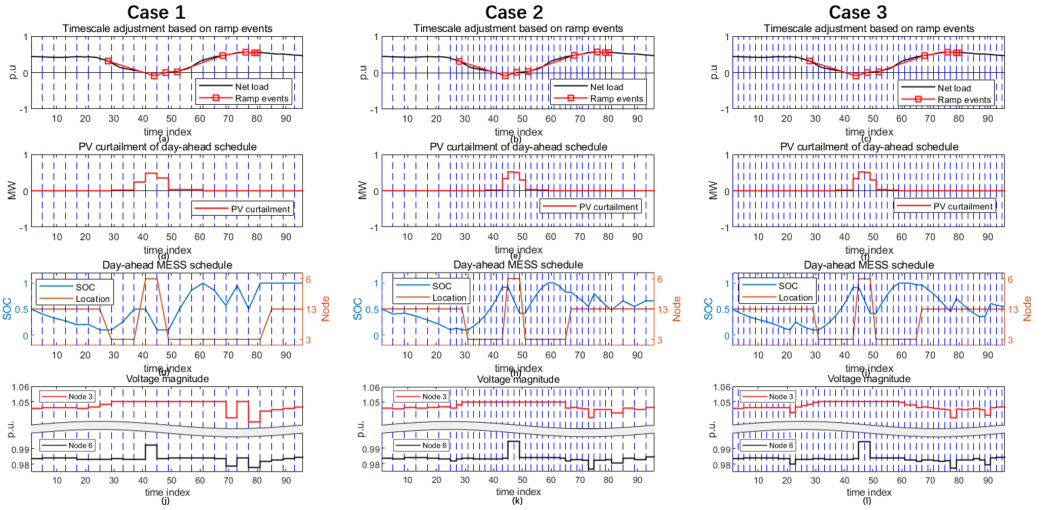

Fig. 8. Day-ahead schedule of typical day in the worst-case scenario. (a), (b), and (c) illustrate the day-ahead forecasted net load, detected ramp events, and optimization timescales for the three cases. (d), (e), and (f) show the PV curtailment. (g), (h), and (i) present the MESS schedule. (j), (k), (l) show the voltage.

Cap." and "PV Cap." represent the obtained installation capacities of MESS and PV, respectively. "LCN", "LVN" and "LST" denote the largest constraint number, largest variable number and largest solving time of the proposed model during the iteration process, respectively. In terms of the planning results, Case 1 gets the cost of $ 15134 with 560 kWh of MESS installation capacity and 697 kW of PV installation capacity. Compared to benchmark (Case 3), Case 1 installs 82 kWh less of MESS and 35 kW less of PV, resulting an additional cost of $ 67 due to increased electricity purchases from the main grid. In contrast, the planning results for Case 2 are identical to those of the benchmark. This shows that selective refinement of timescale leads to more economical and accurate planning results.

Regarding the model size, Case 3 exhibits the highest complexity with the LCN of $28.9*10^3$ and LVN of $22.5*10^3$. In contrast, Case 2 has the LCN of $19.1 * 10^3$ and LVN of $14.0 * 10^3$, approximately 66% and 62% of those of Case 3. Additionally, the LST for Case 2 is approximately 54% of that for Case 3. Therefore, Case 2 demonstrates superior computational efficiency. This highlights that selective refinement helps avoid overly complex model size thus speeding up solving.

Furthermore, we conduct case studies with two MESSs to illustrate the allocation differences in MESS planning. The results are presented in Table IV. Compared to benchmark, Case 1 has installed 35 kWh more of No.1 MESS and 228 kWh less of No.2 MESS. In contrast, the planning results for Case 2 are also entirely consistent with the benchmark. Therefore, this further shows the advantage of selective refinement of timescale in achieving more accurate allocation in planning.

As a side note, the proposed solution approach usually takes only several (no more than 10) iterations to get the converged result. For example, the iteration numbers for three cases of planning with one MESS are 2, 3 and 3, respectively.

To evaluate the performance of the proposed model in scheduling, we conduct case studies for day-ahead scheduling. The installation capacity of MESS and PV are determined by the planning result of Case 2 with one MESS. Three hundred out-of-sample scenarios of historical PV power and loads are

TABLE V
DAY-AHEAD SCHEDULING RESULTS OF TYPICAL DAY OF 13-BUS SYSTEM

	Operation cost ($)	PV Cur. (kWh)	LCN (10^3)	LVN (10^3)	LST (s)
Case 1	8329	1192	2.1	1.6	0.6
Case 2	**6933**	**921**	5.4	3.6	1.9
Case 3	**6933**	**921**	7.8	5.5	3.3

generated as predicted scenarios. The day-ahead scheduling model aims to minimize the operation costs, with constraints aligned with those of the planning model. For illustrative purposes, we present the day-ahead schedule results of a typical day in the worst-case scenario for different cases. The worst-case scenario is defined as the scenario with the smallest net load. The result is depicted in Fig. 8. Fig. 8(a), (b), and (c) illustrate the day-ahead forecasted net load, detected ramp events, and optimization timescales for the three cases. Fig. 8(d), (e), and (f) show the PV curtailment. Fig. 8(g), (h), and (i) present the MESS schedule. Fig. 8(j), (k), and (l) present the voltage magnitude at node 3 and node 6. The operation cost, PV curtailment, LCN, LVN, and LST of day-ahead scheduling model are summarized in Table V. Next, detailed discussions will be presented with a focus on Fig. 8 and Table V.

First, MESS tends to move frequently during periods of over-accumulation events. For instance, as depicted in Fig. 8(h), from 7:00 to 7:30, MESS moves from node 13 to node 3 near the PV for charging. Interestingly, MESS doesn't linger for long and from 10:30 to 11:00, it moves from node 3 to node 6, situated farther away from the PV, for discharging. An hour later, from 12:00 to 12:30, MESS returns from node 6 to node 3 for charging again. This unusual phenomenon reveals that, during peak generation times, MESS may move frequently for PV integration instead of remaining stationary near PV. This is due to grid security constraints and MESS SOC limitation. During the periods of peak PV generation, MESS has to move near the PV for absorption to prevent overvoltage (i.e., node 3). However, due to its limited capacity, MESS may be unable to meet the excessive PV absorption demands. Consequently, to avoid overcharging, MESS has to rapidly move to other nodes with higher voltage safety margins

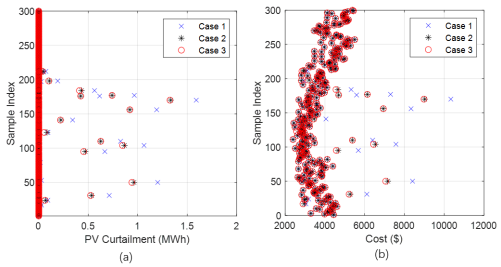

Fig. 9. Day-ahead PV curtailment (a) and cost (b) for three cases of 300 out-of-sample scenarios. Case 1 always gets the highest curtailment and cost. Case 2 gets almost the same levels of curtailment and cost as Case 3.

for discharging (i.e., node 6). After discharging, MESS has to return to the vicinity of PV to resume charging. This highlights that MESS may hit the SOC limits during the periods of over-accumulation events, resulting in frequent movement.

Second, refining the timescale helps reduce PV curtailment. As shown in Table V, Case 1 exhibits the highest level of PV curtailment of 1192 kWh. In contrast, Case 3 gets PV curtailment of 921 kWh, representing a reduction of 22.7% (i.e., 22.7% = (1192-921)/1192). This is due to the finer-grained scheduling of MESS movement. It reduces the time MESS spends in idle mode and fully utilizes its charging and discharging capacities. As shown in Fig. 8, it is observed that PV curtailment occurs when MESS frequently moves at noon. The scheduling time resolution of MESS is 1 h of Case 1, which is twice the actual travel time between each node. Consequently, MESS spends more idle time in Case 1, resulting in a larger PV curtailment.

Third, refining the timescale selectively has the potential to achieve the same level of PV curtailment and cost as the fully fine resolution. As shown in Table V, despite Case 2 having LCN, LVN and LST of about 69%, 65% and 58% of those of Case 3, they both get the identical PV curtailment with 921 kWh and operation cost with $ 6933. This is mainly because PV curtailment occurs during ramp events, and Case 2 precisely refines the timescale during these ramp events. It implies that the timescale during curtailment periods for both Case 2 and Case 3 is likely to be the same. Consequently, the scheduling granularity for MESS's movement in Case 2 and Case 3 is likely to be consistent, enabling Case 2 to approach the benchmark solution. As shown in Fig. 8(e) and (h), Case 2 refines the timescale from 6:00 to 20:00, while PV curtailment occurs from 9:00 to 14:30. Additionally, the timescale when MESS moves is 30 minutes in both Case 2 and Case 3.

PV curtailment and cost for 300 out-of-sample scenarios are shown in Fig. 9. It is observed that 15 samples experience significant PV curtailment. Among them, Case 1 always gets the highest curtailment. Case 2 and Case 3 get almost identical levels of curtailment. These results highlight again the superiority of the proposed model.

2) Sensitivity Analysis: The sensitivity studies are performed to investigate the impact of parameters of ramping event detection on interval number and cost, as shown in Fig. 10. According to the simulation results, there are three observations: (1) Interval number is generally negatively correlated with $\mathcal{Z}_m$, $\mathcal{Z}_c$, $\mathcal{W}$ and ρ_2. (2) Interval number is generally positively correlated with Γ, $\bar{t}$ and ν. (3) Interval number

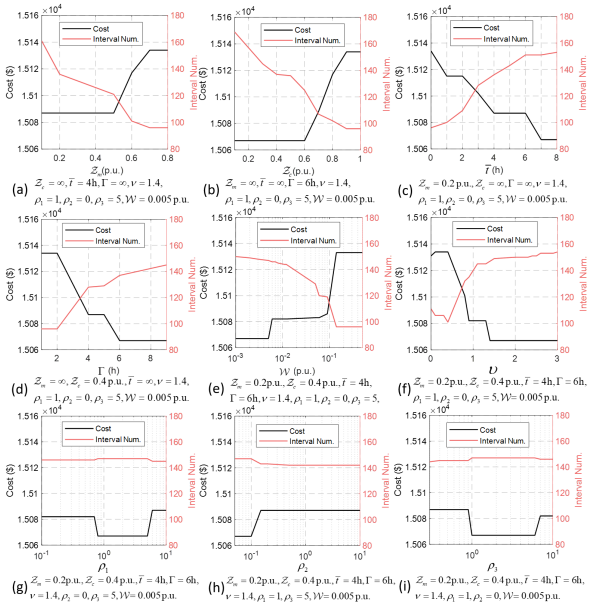

Fig. 10. Cost and adjusted interval number versus the ramp event detection parameters (a)$\mathcal{Z}_m$, (b)$\mathcal{Z}_c$, (c)$\bar{t}$, (d)Γ, (e)$\mathcal{W}$, (f)ν, (g)ρ_1, (h)ρ_2, and (i)ρ_3.

TABLE VI
COMPARISON WITH THE DUALITY-BASED SOLUTION APPROACH

Uncertainty bound (p.u.)	0.05	0.1	0.15	0.2	0.25	0.3
Cost obtained by DSA ($)	13954	14327	14751	15134	15645	16610
Cost obtained by HSA ($)	13954	14327	14751	15134	15645	16678
Solving time of DSA (s)	102	174	111	112	157	203
Solving time of HSA (s)	24	23	21	14	36	34

increases first and then decreases with ρ_1 and ρ_3. That is mainly because parameter modification leads to the change of detected event number. For instance, R_1 (17) becomes stronger with the increase of $\mathcal{Z}_m$, resulting in fewer detected ramp events. Thus, the interval number decreases. Although the low time resolution reduces the model size, it could also increase the cost due to the reduced feasible region or flexibility. Hence, it is important to balance the model size and solution quality when selecting these parameters. We present a group of proper parameters in Table II. It shows effectiveness and consistency in our simulations. According to the requirement of different realistic problems, these parameters can be further adjusted based on the sensitivity analysis results to enhance the performance.

3) Performance of the Solution Approach: To show the effectiveness of the proposed hybrid solution approach (HSA), we compare the solution time and the cost of planning and operation with the duality-based solution approach (DSA) [27], as presented in Table VI. We use the timescale with 1 h as an instance. In DSA, (P3) is firstly recast based on SAP. Then it is reformulated into a mixed integer linear program (MILP) problem based on duality theory and solved by Gurobi directly. It is observed that HSA achieves good performance in all test cases. For uncertainty bound < 0.3 p.u., HSA gets cost entirely consistent with DSA. The error of cost is at most 0.4% (i.e., $0.4\% \approx (16678 - 16610)/16610$) for uncertainty bound $= 0.3$ p.u. Moreover, the solution time of HSA is less than 23.5% of that of DSA (i.e., $23.5\% \approx 24/102$). These results highlight the superiority of HSA. As a side note, the

TABLE VII
THE IMPACTS OF SELLING ELECTRICITY TO THE MAIN GRID

	Unidirectional power flow	Selling price of $ 100/MWh	Selling price of $ 200/MWh
Cost ($)	13196	11437	11114
Selling energy (MWh)	0	3.229	3.251

TABLE VIII
SOLUTION RESULTS UNDER DIFFERENT PENALTY COST SETTINGS

Penalty cost	$ 5/kWh	$ 2/kWh	$ 1/kWh	$ 0.5/kWh	$ 0.4/kWh
Cost ($)	16544	16543	16532	16310	16100
PV Cur. (kWh)	0	3	27	1051	1821
Load Shed. (kWh)	0	0	110	526	531

TABLE IX
IMPACT OF RAMP RULE $R_1^*(t_s, t_e)$

Ramp rules	Num. of time periods	Operation cost ($)	LCN (10^3)	LVN (10^3)	LST (s)
$R_1(t_s,t_e) + R_2(t_s,t_e)$	30	3002	3.8	2.5	0.57
$R_1^*(t_s,t_e) + R_2(t_s,t_e)$	35	2927	4.8	3.2	0.87

TABLE X
PLANNING RESULTS OF 141-BUS SYSTEM

	Cost ($)	MESS Total Cap. (MWh)	PV Total Cap. (MW)	LCN (10^3)	LVN (10^3)	LST (s)
Case 1	165335	7.876	8.940	21.6	16.6	13
Case 2	**164619**	7.583	9.092	40.1	33.0	50
Case 3	**164619**	7.583	9.092	63.1	51.9	155

iteration numbers of HSA for these cases are 3, 2, 4, 2, 7, 7.

4) Impact of Selling Electricity to the Main Grid: In this subsection, the impacts of three electricity-selling settings are compared, as shown in Table VII. In this study, the voltage ratios of the two transformers are adjusted to 1:1.04 and 1:1.05, respectively. Compared to the unidirectional power flow, selling electricity to the main grid could achieve a cost saving of $ 1759 (i.e., 1759=13196-11437) when the selling price is $ 100/MWh. Besides, the cost saving expands when the selling price increases to $ 200/MWh.

5) Impact of Penalty Cost for PV Curtailment and Load Shedding: In this study, the base load is adjusted to 110%. Table VIII shows the cost, PV curtailment and load shedding under the five penalty cost settings. PV curtailment and load shedding increase with the decrease in penalty cost. Meanwhile, the cost decreases from $ 16544 to $ 16100.

6) Impact of Ramp Rule $R_1^*(t_s, t_e)$: Table IX shows the day-ahead operation cost, number of time periods, LCN, LVN, LST for the proposed model based on different ramp rules. In this study, the day-ahead forecast net load for a typical day is used, and $\mathcal{Z}_m$ is set to 0.4 p.u. It shows that ramp rule $R_1^*(t_s,t_e)+R_2(t_s,t_e)$, which accounts for uncertainty, enables the detection of more ramp events and increases the number of time periods from 30 to 35. This refinement leads to a larger model size, but it simultaneously reduces the operation cost by $75 (i.e., 75=3002-2927). This result illustrates that accounting for uncertainty in the detection algorithm could further enhance the accuracy of the variable timescale model.

B. 141-Bus Distribution Network

The 141-bus distribution feeder includes 84 load nodes with the peak being 11.9 MW and 7.4 MVar [28]. The apparent power capacity of the branch is 20 MVA. Utility-scale PVs are to be installed at nodes 78-82. There are two MESSs and five MESS candidate locations in the system. The initial and terminal node are node 141. The voltage ratios of transformers are set to 1:1.03, 1:1.01 and 1:1.01, respectively. The planning results of the three cases are shown in Table X. Case 2 obtains planning results entirely consistent with the benchmark. Moreover, LCN, LVN and LST for Case 2 are 64%, 64% and 32% of the benchmark, respectively. Despite Case 1 having the fastest LST of 13 s, its planning results exhibit significant discrepancies compared to the benchmark. The results demonstrate the superiority of the proposed ramping-based variable timescale model again.

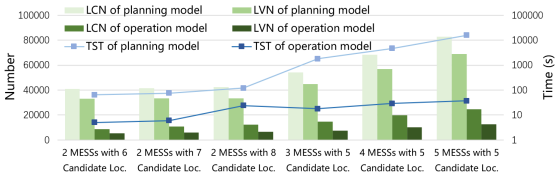

Fig. 11. Scalability analysis of the proposed method in 141-bus system.

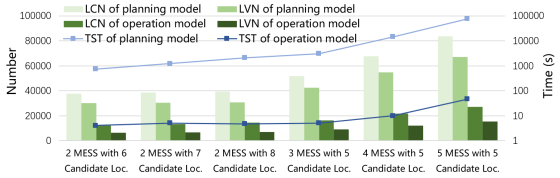

Fig. 12. Scalability analysis of the proposed method in 906-bus system.

We also perform a scalability analysis of the proposed model in the 141-bus system for different numbers of MESSs and MESS candidate locations. The LCN, LVN and total solving time (TST) of planning and operation model are shown in Fig. 11. It is shown that the size and solving time of the proposed model are not apparently sensitive to the number of MESS candidate locations. Besides, as the MESS number increases, the model size increases linearly rather than quadratically or exponentially. This indicates that it will not have computer memory issue when solving the planning problems with multiple MESSs. Moreover, the solution time of the operation model is not apparently sensitive to the number of MESS. It remains within 100 s, which can fully satisfy the timeliness requirement for day-ahead operation scheduling.

C. 906-Bus Distribution Network

Finally, we add a 906-bus low-voltage distribution system to verify the scalability of the proposed model in large-scale distribution network. The feeder includes 905 distribution lines and 55 load nodes with the peak being 41.9 kW and 13.8 kVar. The apparent power capacity of the branch is 60 kVA. PVs are to be installed at nodes 891-895. The travel time between each MESS candidate location is 30 min. The results of scalability analysis are shown in Fig. 12. Thanks to the constraints screening technology, the LCN and LVN of the proposed model in the 906-bus and 141-bus systems are almost identical. For example, in the case of 5 MESSs and 5 MESS candidate locations, the planning model's LCN is 83570 for 906-bus system and 82928 for 141-bus system. Besides, the solution time of the operation model also remains

within 100 s. Given the scalability analysis of the proposed methods, we believe that the proposed model is promising for practical implementation in real-world distribution systems with multiple MESSs and candidate locations.

VII. Conclusion

This paper introduces a novel variable timescale model for planning-operation co-optimization. A novel ramp event detection algorithm has been developed to facilitate timescale adjustments. Additionally, we propose a multistage optimization model with a variable uncertainty set to ensure solution nonanticipativity and robustness. We also present a novel hybrid solution approach to solve the model. Simulations have been conducted using the 13-bus system, 141-bus system, and 906-bus system. The methods proposed exhibit promising accuracy and computational efficiency. In future studies, we intend to explore heuristic neural network learning and multi-agent techniques to further enhance the model.

References

[1] A. Samadi, L. Soder, E. Shayesteh, and R. Eriksson, "Static equivalent of distribution grids with high penetration of pv systems," *IEEE Trans. on Smart Grid*, vol. 6, no. 4, pp. 1763–1774, Jul. 2015.

[2] X. Chen, W. Wu, and B. Zhang, "Robust capacity assessment of distributed generation in unbalanced distribution networks incorporating anm techniques," *IEEE Trans. on Sustainable Energy*, vol. 9, no. 2, pp. 651–663, Apr. 2018.

[3] Ángel Molina-García, R. A. Mastromauro, T. García-Sánchez, S. Pugliese, M. Liserre, and S. Stasi, "Reactive power flow control for pv inverters voltage support in lv distribution networks," *IEEE Trans. on Smart Grid*, vol. 8, no. 1, pp. 447–456, Jan. 2017.

[4] S. Wang, S. Chen, L. Ge, and L. Wu, "Distributed generation hosting capacity evaluation for distribution systems considering the robust optimal operation of oltc and svc," *IEEE Trans. on Sustainable Energy*, vol. 7, no. 3, pp. 1111–1123, Jul. 2016.

[5] A. Soroudi, A. Rabiee, and A. Keane, "Distribution networks' energy losses versus hosting capacity of wind power in the presence of demand flexibility," *Renewable Energy*, vol. 102, pp. 316–325, Mar. 2017.

[6] H. M. A. Ahmed, H. F. Sindi, M. A. Azzouz, and A. S. A. Awad, "Optimal sizing and scheduling of mobile energy storage toward high penetration levels of renewable energy and fast charging stations," *IEEE Trans. on Energy Conversion*, vol. 37, no. 2, pp. 1075–1086, Jun. 2022.

[7] J. Kim and Y. Dvorkin, "Enhancing distribution system resilience with mobile energy storage and microgrids," *IEEE Trans. on Smart Grid*, vol. 10, no. 5, pp. 4996–5006, Sept. 2019.

[8] S. Wang and R. Bo, "A resilience-oriented multi-stage adaptive distribution system planning considering multiple extreme weather events," *IEEE Trans. on Sust. Energy*, vol. 14, no. 2, pp. 1193–1204, Apr. 2023.

[9] Z. Lu, X. Xu, Z. Yan, and M. Shahidehpour, "Multistage robust optimization of routing and scheduling of mobile energy storage in coupled transportation and power distribution networks," *IEEE Trans. on Transp. Elect.*, vol. 8, no. 2, pp. 2583–2594, Jun. 2022.

[10] X. Liu, C. B. Soh, T. Zhao, and P. Wang, "Stochastic scheduling of mobile energy storage in coupled distribution and transportation networks for conversion capacity enhancement," *IEEE Trans. on Smart Grid*, vol. 12, no. 1, pp. 117–130, Jan. 2021.

[11] Y. Sun, J. Zhong, Z. Li, W. Tian, and M. Shahidehpour, "Stochastic scheduling of battery-based energy storage transportation system with the penetration of wind power," *IEEE Trans. on Sustainable Energy*, vol. 8, no. 1, pp. 135–144, Jan. 2017.

[12] S. Y. Kwon, J. Y. Park, and Y. Kim, "Optimal v2g and route scheduling of mobile energy storage devices using a linear transit model to reduce electricity and transportation energy losses," *IEEE Trans. on Industry Applications*, vol. 56, no. 1, pp. 34–47, Jan.-Feb. 2020.

[13] W. Wang, X. Xiong, Y. He, J. Hu, and H. Chen, "Scheduling of separable mobile energy storage systems with mobile generators and fuel tankers to boost distribution system resilience," *IEEE Tran. on Smart Grid*, vol. 13, no. 1, pp. 443–457, Jan. 2022.

[14] J. Deane, G. Drayton, and B. Ó. Gallachóir, "The impact of sub-hourly modelling in power systems with significant levels of renewable generation," *Applied Energy*, vol. 113, pp. 152–158, Jan. 2014.

[15] E. Nycander, G. Morales-España, and L. Söder, "Capacity and intra-hour ramp reserves for wind integration," *IEEE Trans. on Sustainable Energy*, vol. 13, no. 3, pp. 1430–1443, Jul. 2022.

[16] S. Pineda, R. Fernández-Blanco, and J. M. Morales, "Time-adaptive unit commitment," *IEEE Trans. on Power Systems*, vol. 34, no. 5, pp. 3869–3878, Sept. 2019.

[17] J. Yan, Y. Li, J. Yao, S. Yang, F. Li, and K. Zhu, "Look-ahead unit commitment with adaptive horizon based on deep reinforcement learning," *IEEE Trans. on Power Systems*, vol. 39, no. 2, pp. 3673–3684, Mar. 2024.

[18] M. Zhang, Z. Yang, W. Lin, J. Yu, W. Dai, and E. Du, "Enhancing economics of power systems through fast unit commitment with high time resolution," *Applied Energy*, vol. 281, p. 116051, Jan. 2021.

[19] M. Cui, J. Zhang, A. R. Florita, B.-M. Hodge, D. Ke, and Y. Sun, "An optimized swinging door algorithm for identifying wind ramping events," *IEEE Trans. on Sust. Energy*, vol. 7, no. 1, pp. 150–162, Jan. 2016.

[20] M. Cui, D. Ke, Y. Sun, D. Gan, J. Zhang, and B.-M. Hodge, "Wind power ramp event forecasting using a stochastic scenario generation method," *IEEE Trans. on Sust. Energy*, vol. 6, no. 2, pp. 422–433, Apr. 2015.

[21] R. Sevlian and R. Rajagopal, "Detection and statistics of wind power ramps," *IEEE Trans. on Power Systems*, vol. 28, no. 4, pp. 3610–3620, Nov. 2013.

[22] W. Zhu, L. Zhang, M. Yang, and B. Wang, "Solar power ramp event forewarning with limited historical observations," *IEEE Trans. on Industry Applications*, vol. 55, no. 6, pp. 5621–5630, Nov. 2019.

[23] Y. Zhou, Q. Zhai, and L. Wu, "Multistage transmission-constrained unit commitment with renewable energy and energy storage: Implicit and explicit decision methods," *IEEE Trans. on Sustainable Energy*, vol. 12, no. 2, pp. 1032–1043, Apr. 2021.

[24] A. Lorca and X. A. Sun, "Multistage robust unit commitment with dynamic uncertainty sets and energy storage," *IEEE Trans. on Power Systems*, vol. 32, no. 3, pp. 1678–1688, May 2017.

[25] A. Lorca, X. A. Sun, E. Litvinov, and T. Zheng, "Multistage adaptive robust optimization for the unit commitment problem," *Operations Research*, vol. 64, no. 1, pp. 32–51, Feb. 2016.

[26] Q. Zhai, X. Li, X. Lei, and X. Guan, "Transmission constrained uc with wind power: An all-scenario-feasible milp formulation with strong nonanticipativity," *IEEE Trans. on Power Systems*, vol. 32, no. 3, pp. 1805–1817, May 2017.

[27] H. Ye, "Surrogate affine approximation based co-optimization of transactive flexibility, uncertainty, and energy," *IEEE Trans. on Power Systems*, vol. 33, no. 4, pp. 4084–4096, Jul. 2018.

[28] L. Zhang, H. Ye, F. Ding, Z. Li, and M. Shahidehpour, "Increasing pv hosting capacity with an adjustable hybrid power flow model," *IEEE Trans. on Sustainable Energy*, vol. 14, no. 1, pp. 409–422, Jan. 2023.

[29] M. Nazemi, P. Dehghanian, X. Lu, and C. Chen, "Uncertainty-aware deployment of mobile energy storage systems for distribution grid resilience," *IEEE Trans. on Smart Grid*, vol. 12, no. 4, pp. 3200–3214, Jul. 2021.

[30] M. E. Baran and F. F. Wu, "Network reconfiguration in distribution systems for loss reduction and load balancing," *IEEE Trans. on Power Delivery*, vol. 4, no. 2, pp. 1401–1407, Apr. 1989.

[31] X. Xu, J. Li, Z. Xu, J. Zhao, and C. S. Lai, "Enhancing photovoltaic hosting capacity-a stochastic approach to optimal planning of static var compensator devices in distribution networks," *Applied Energy*, vol. 238, pp. 952–962, Mar. 2019.

[32] G. E. Williams, "Critical aperture convergence filtering and systems and methods thereof," US, US7076402 B2[P]. 2006.

[33] Y. Zhou, Q. Zhai, and L. Wu, "Optimal operation of regional microgrids with renewable and energy storage: Solution robustness and nonanticipativity against uncertainties," *IEEE Trans. on Smart Grid*, vol. 13, no. 6, pp. 4218–4230, Nov. 2022.

[34] S. Zhang, H. Ye, F. Wang, Y. Chen, S. Rose, and Y. Ma, "Data-aided offline and online screening for security constraint," *IEEE Trans. on Power Systems*, vol. 36, no. 3, pp. 2614–2622, 2021.

[35] S. Boyd and L. Vandenberghe, *Convex Optimization*. Cambridge, U.K.: Cambridge Univ. Press, 2009.

[36] Material of single-phase ieee 13-bus distribution system. Nov. 2017. [Online]. Available: https://github.com/hafezbazrafshan/single-phase-feeders

[37] "IEEE PES Test Feeder," 2024. [Online]. Available: https://cmte.ieee.org/pes-testfeeders/resources/

[38] "Open Power System Data," 2020. [Online]. Available: https://data.open-power-system-data.org/time_series/2020-10-06